

Intracellular Mechanical Drugs Induce Cell-Cycle Altering and Cell Death

María Isabel Arjona, Marta Duch, Alberto Hernández-Pinto, Patricia Vázquez, Juan Pablo Aguil, Rodrigo Gómez-Martínez, Mariano Redondo-Horcajo, Ezhil Amirthalingam, Lluïsa Pérez-García, Teresa Suárez,* and José A. Plaza*

Current advances in materials science have demonstrated that extracellular mechanical cues can define cell function and cell fate. However, a fundamental understanding of the manner in which intracellular mechanical cues affect cell mechanics remains elusive. How intracellular mechanical hindrance, reinforcement, and supports interfere with the cell cycle and promote cell death is described here. Reproducible devices with highly controlled size, shape, and with a broad range of stiffness are internalized in HeLa cells. Once inside, they induce characteristic cell-cycle deviations and promote cell death. Device shape and stiffness are the dominant determinants of mechanical impairment. Device structural support to the cell membrane and centering during mitosis maximize their effects, preventing spindle centering, and correct chromosome alignment. Nanodevices reveal that the spindle generates forces larger than 114 nN which overcomes intracellular confinement by relocating the device to a less damaging position. By using intracellular mechanical drugs, this work provides a foundation to defining the role of intracellular constraints on cell function and fate, with relevance to fundamental cell mechanics and nanomedicine.

physical terms, the combination of cell membrane–cortex system and cytoskeleton constitutes a mechanical system whose stability is based on a force balance between compression and tensile-load-bearing components.^[1] Any physical perturbation of this cellular mechanical system elicits a redistribution of forces and rearrangement of mechanical elements that can be disruptive.^[3] Thus, it is not surprising that multiple chemical drugs for research and therapeutics target to alter the cellular mechanical performance. Anticancer drugs such as paclitaxel or colchicine affect the microtubules, provoking mitotic catastrophe to cause cell death.^[4,5] Other compounds, including cytochalasin B, cytochalasin D, and latrunculin A disrupt actin filaments, also disturbing cell function and growth.^[6]


Intracellular mechanical cues induced by physiological internalization of large

objects can also alter the redistribution of forces and the rearrangement of mechanical elements. Indeed, during entosis (the engulfment of one living cell by another), cytokinesis in the engulfing cell is perturbed, which can cause aneuploidy.^[7,8] This has parallels to cell division perturbation when cells are exposed to natural or artificial “long” fibrous material such as asbestos fibers that can induce genomic changes and cancer by sterically blocking cytokinesis.^[9]

1. Introduction

It is increasingly clear that physical and chemical features of the cell are both fundamental to function and development. The cell's cytoskeleton, composed of microtubules, actin filaments, and intermediate filaments, is an active structure associated with mechanical function and is thus involved in many fundamental processes during the cell cycle.^[1,2] In

M. I. Arjona, M. Duch, J. P. Aguil, R. Gómez-Martínez, J. A. Plaza
Instituto de Microelectrónica de Barcelona
IMB-CNM (CSIC)
Campus UAB
Cerdanyola del Vallès, Barcelona 08193, Spain
E-mail: joseantonio.plaza@imb-cnm.csic.es

 The ORCID identification number(s) for the author(s) of this article can be found under <https://doi.org/10.1002/adma.202109581>.

© 2022 The Authors. Advanced Materials published by Wiley-VCH GmbH. This is an open access article under the terms of the Creative Commons Attribution-NonCommercial-NoDerivs License, which permits use and distribution in any medium, provided the original work is properly cited, the use is non-commercial and no modifications or adaptations are made.

A. Hernández-Pinto, P. Vázquez, M. Redondo-Horcajo, T. Suárez
Centro de Investigaciones Biológicas Margarita Salas
CIB (CSIC)
Madrid 28040, Spain
E-mail: teresa@cib.csic.es

E. Amirthalingam, L. Pérez-García
Departament de Farmacologia
Toxicologia i Química Terapèutica and Institut de Nanociència i
Nanotecnologia (IN2UB)
Universitat de Barcelona
Barcelona 08028, Spain

L. Pérez-García
School of Pharmacy
University of Nottingham
Nottingham NG7 2RD, UK

DOI: 10.1002/adma.202109581

Understanding how internal mechanical perturbation by internalized particles can affect the cell cycle has relevance not only to fundamental mechanobiology, but also to micro- and nanotoxicity in nanomedicine. However, how intracellular mechanical perturbations alter the cell cycle still remains elusive. Here, we have established how intracellular reinforcements, hindrance blocking, and structural supports on cell membrane induced by internalized physical structures mechanically affect the cell cycle and contribute to cell death.

2. Design and Fabrication of High-Aspect-Ratio Intracellular Mechanical Drugs

We predicted that internalized mechanical drugs with precisely prescribed shape and dimensions in the range of the cell mitotic diameter ($\Phi_{\text{HeLa}} = 20.9 \pm 0.6 \mu\text{m}$) would destabilize cell mechanics during mitosis, allowing us to study intracellular reinforcements and constraints. To assist the internalization of these large objects, we extended our experience in the internalization of smaller polysilicon devices by HeLa cells^[10–12] and the fact that many cell types favor “tip-first” internalization of 1D materials.^[13] Accordingly, we designed high-aspect-ratio 8-pronged star-shaped devices that mimic 1D structures, measuring $23.5 \mu\text{m}$ in diameter (Φ) and 500 nm thick (t), and comprising cantilevers measuring $10 \mu\text{m}$ long (L) and $1.5 \mu\text{m}$ wide (W) (Figure 1a); we refer to these as SL-500 devices.

These studies required mass production of biocompatible devices with highly reproducible shape, dimensions, and material properties.^[14] Following these requirements, we used silicon technologies allowing the fabrication of high-aspect-ratio polysilicon devices that can be precisely patterned at micro- and nanoscales and have been used successfully to probe intracellular mechanical processes.^[12,15] Moreover, the inherent biocompatibility of silicon-based devices^[16] has allowed the internalization and the microinjection of silicon-based chips by cells and embryos.^[11,12,15,17] The fabrication technology is similar to that previously reported for intracellular silicon chip production,^[10,11] whose biocompatibility have been proven. Briefly, a $1 \mu\text{m}$ -thick silicon oxide layer is deposited onto a silicon substrate (Figure 1b and Figure S1 and the Experimental Section (Supporting Information)) as sacrificial layer. Onto this, a structural polysilicon layer is deposited whose thickness defines the thickness of the devices. A photolithographic step and subsequent polysilicon etching pattern the chips (Figure 1c). Finally, the devices were released from the substrate by etching the sacrificial silicon oxide layer (Figure 1d) and were collected and suspended in 96% ethanol to prevent the contamination of the samples (Figure 1b and Movie S1 (Supporting Information)). The technology allowed the batch fabrication of more than 7 million identical devices on a 4 in. silicon wafer. The high geometric reproducibility of the fabricated devices, $\Phi = 23.27 \pm 0.01 \mu\text{m}$ and $t = 4870 \pm 1.2 \text{ nm}$ (Figure S2, Supporting Information) allows the challenge in studying cell mechanobiology

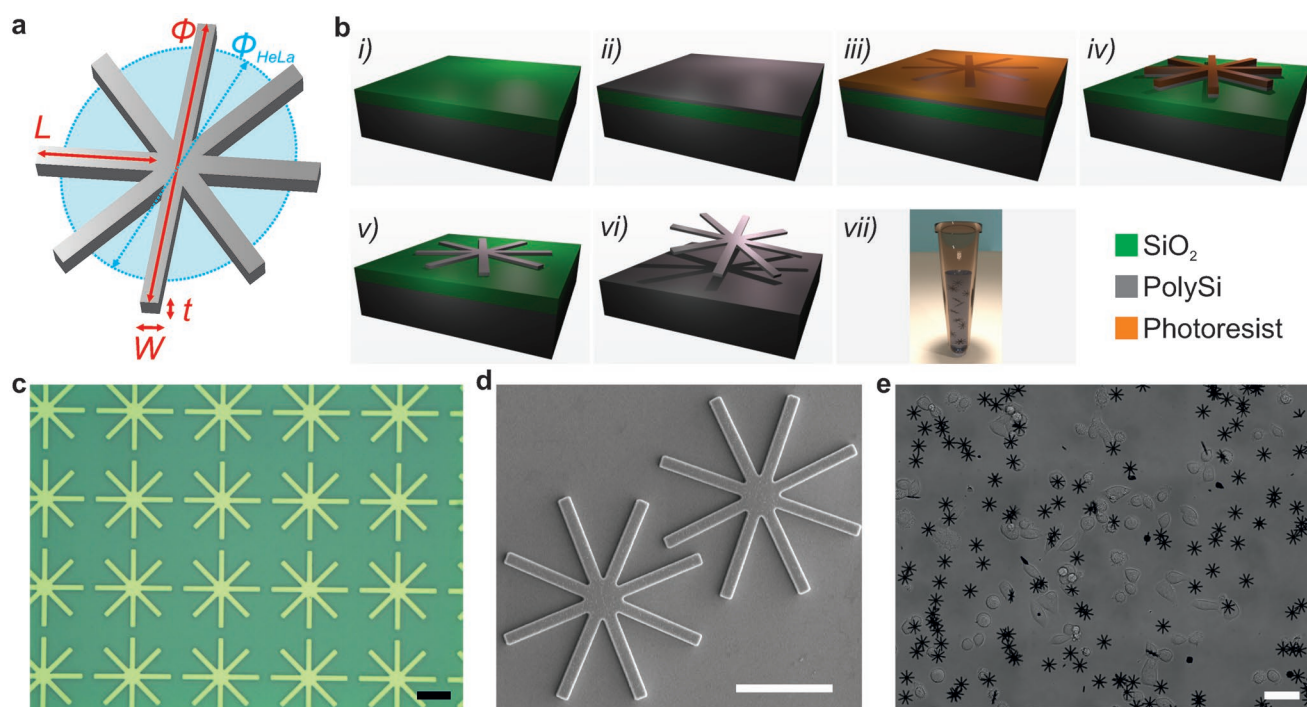


Figure 1. Design and fabrication of intracellular mechanical drugs. a) Schematic of the 8-pronged star showing the definition of main geometrical parameters (t = thickness, w and L = cantilever’s width and length, Φ = device diameter, Φ_{HeLa} = mitotic diameter of a HeLa cell). b) Schematic of the technology. i) A $1 \mu\text{m}$ -thick silicon oxide layer (green) is grown on a silicon substrate. ii) A polysilicon layer is deposited as a structural layer. iii) A photolithographic process defines the shape of the chips. iv) Photoresist is striped and polysilicon dry etched to pattern the device. v) Photoresist is removed. vi) Silicon oxide sacrificial etching to release the chips. vii) Released chips are immersed on ethanol and collected in an Eppendorf. c) Optical image of the chips at wafer level. d) Scanning electron microscopy (SEM) images of the released chips. e) Optical images of HeLa cells cocultured with the devices. Scales bars = $10 \mu\text{m}$ (c,d) and $50 \mu\text{m}$ (e).

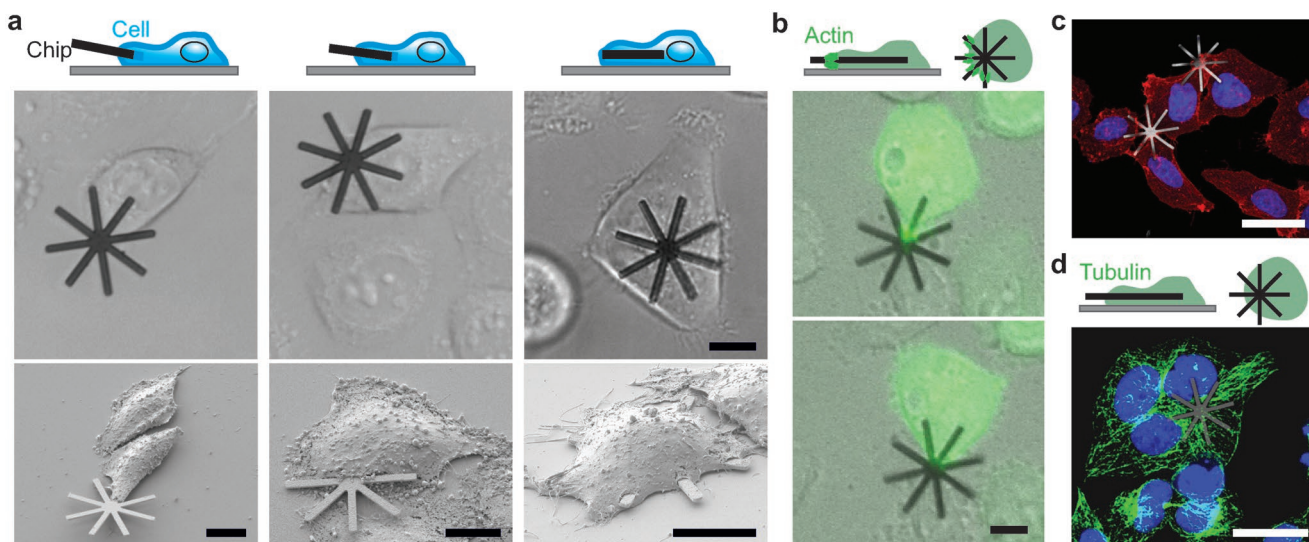


Figure 2. Device internalization by HeLa. a) Schematic (top), optical images of living HeLa cells (middle), and SEM images (bottom) of fixed cells internalizing SL-500 devices. b) Schematic (top) and fluorescence images of HeLa living cells showing actin (green) enrichment in the interaction with SL-500 devices. c) Fluorescence images of cell membrane (red) in HeLa fixed cells with internalized SL-500 devices. d) Schematic (top) and fluorescence images of β -tubulin (green) in HeLa fixed cells with internalized SL-500 devices. Cell nuclei are blue in (c) and (d). Scales bars = 10 μ m (a,b) and 25 μ m (c,d).

to be circumvented by providing tools with exquisitely well-controlled physical properties.

3. High Rate of SL-500 Device Internalization by HeLa Cells

We initially used the human cervical carcinoma HeLa cell line, a model routinely used in human cell biology and cancer research.^[18] To facilitate SL-500 internalization, HeLa cells were incubated in small volumes with devices, Figure 1e, with a minimum cell:device ratio of 2:1 (Experimental Section, Supporting Information). Notwithstanding a total apparent SL-500 weight of 0.73 pN (Figure S3, Supporting Information), we anticipated that HeLa cells would successfully engage with the devices. To analyze cell behavior thoroughly, we followed the interaction of individual HeLa cells with an associated single SL-500 device in one-to-one mode by time-lapse microscopy (Experimental Section, Supporting Information).

Despite the large diameter of the devices, $86.51 \pm 5.29\%$ HeLa cells partially or totally internalized nearby devices, typically by catching the proximal arm of the star (Figure 2a and Movie S2 (Supporting Information)), corroborating the prediction that a design sharing feature with a 1D structure would show tip-first internalization. We also observed actin-based protrusions extending along the target, a characteristic of phagocytosis^[19] (Figure 2b and Movie S3 (Supporting Information)). Recent work suggests that phagocytosis by nonprofessional phagocytes is a general feature of normal tissue cells.^[20] Moreover, plasma membrane surrounded the devices in the places where they pierce the cell (Figure 2c). Contrary, we found no evidence of direct interaction between the SL-500 devices and microtubules (Figure 2d), consistent with the behavior of polysilicon devices microinjected within mouse embryos.^[15]

4. Intracellular Mechanical Drugs Alter Cell Division and Provoke Cell Death

SL-500 internalization altered the cell cycle and ultimately caused cell death (Figure 3a–c and Figure S4 (Supporting Information)). To characterize this, we followed the behavior of HeLa cells with partially or totally internalized SL-500 devices for 24 h, a period that includes at least one cell division (HeLa cell doubling time: 18.0 ± 0.5 h). We found that 90.38% of cells with totally internalized SL-500 exhibited the hallmarks of mechanically altered cell cycle (MACC) (Figure 3d), including 55.32% with delayed or blocked mitosis, 25.53% that failed to execute cytokinesis, and 19.15% undergoing asymmetric division (Figure 3e and Figures S4 and S5 and Movie S4 (Supporting Information)). During this observation period, $31.35 \pm 9.98\%$ of HeLa cells with internalized SL-500 died, compared to <1% of cells lacking devices (Figure 3b,c,f and Movie S5 (Supporting Information)). This suggests that cell death was a direct consequence of star device internalization and, more often, subsequent MACC.

4.1. Intracellular Mechanical Device Shape Is a Major Determinant of Cell Damage

We wished to delineate the mechanical basis of the cell-cycle interference and cell death induced by the intracellular constraints, reinforcements, and supports and we reasoned that perturbation may depend on physical constraint effects on the cytoplasm. To test this hypothesis, we designed and fabricated devices with varying shapes (star (S) and disk (D)) and Φ (23.5 μ m (L) and 13.7 μ m (s)), and with varying thicknesses (50, 110, 230, and 500 nm) (Figure 4a and Figures S1 and S3 (Supporting Information)). Maximal hindrance is predicted for devices with larger diameters and in-plane areas (Figure 4b).

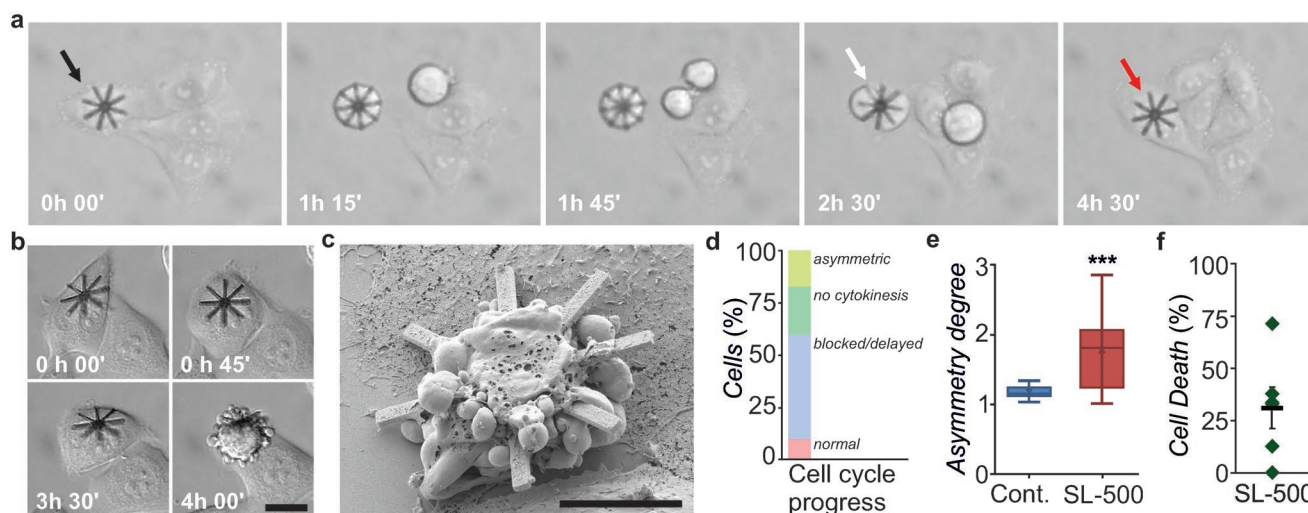


Figure 3. Intracellular SL-500 promotes MACC and cell death on HeLa cells. a) Optical images from a time lapse experiment showing a HeLa cell with an internalized SL-500 device (black arrow) with blocked mitosis (white arrow) and failed cytokinesis (red arrow). The nearby cell divides normally. b) Still optical images from a time lapse experiment showing a HeLa cell with an internalized SL-500 device that causes cell death. c) SEM image of a dead cell with an internalized SL-500 device. d) Percentage of MACC categories of HeLa cells with internalized SL-500 devices. e) Mitotic asymmetry induced by internalized SL-500 devices in HeLa cells versus normal cells, $p = 0.0009$ (Mann–Whitney U test). f) Cell death percentage of HeLa cells with internalized SL-500 devices. Each dot (f) represents an independent experiment where individual cells were followed for 24 h and the outcome plotted (Experimental Section, Supporting Information). The horizontal black line represents the mean \pm standard error of the mean (s.e.m.). Scale bars = 20 μm (a) and 10 μm (b,c). Total number of analyzed cells, $n = 33\text{--}48$.

Ss-500 and Ds-500 devices exhibited high internalization rates, similar to those of the SL-500 devices ($76.11 \pm 9.31\%$ and $73.89 \pm 7.84\%$, respectively; Figure 4c and Figure S6 (Supporting Information)). We observed that DL-500, a disk device whose diameter ($23.45 \pm 0.02 \mu\text{m}$) is larger than that of the mitotic radius, was also internalized (Figure 4d and Figure S6 (Supporting Information)), albeit at a lower frequency than SL-500 ($18.53 \pm 3.14\%$ vs $86.51 \pm 5.29\%$; $p = 0.0001$). Clearly, HeLa cells have difficulties internalizing large 2D disks such as DL-500, and this probably reflects the need for extensive morphological remodeling, as the device surface area represents $\approx 66\%$ of the cell surface area (Figure S3, Supporting Information). Internalization of chips with lateral dimensions of 25 μm has been described for different cell lines.^[21] Conversely, on phagocytic cells, it has been suggested that the total surface area of the

internalized devices, rather than their volume, determines the maximum load due to the additional membrane required for envelopment.^[22]

Our results show that HeLa cells favored the internalization of large devices with features akin to pseudo-1D structures, as with the star design. This suggests that particle shape plays a dominant role in internalization by HeLa cells, a phenomenon also reported in professional phagocytes.^[23]

Internalized DL-500 devices exerted major MACC (Figure 4e), inducing nearly 90% cell death (Figure 4f). This may reflect their tendency to locate centrally during cell division. By contrast, Ss-500 and Ds-500 devices generated smaller MACC ($28.00 \pm 12.94\%$ and $40.40 \pm 11.13\%$, respectively) (Figure 4e) and less cell death ($9.25 \pm 5.96\%$ and $16.19 \pm 8.46\%$, respectively; Figure 4f). During cell division, when

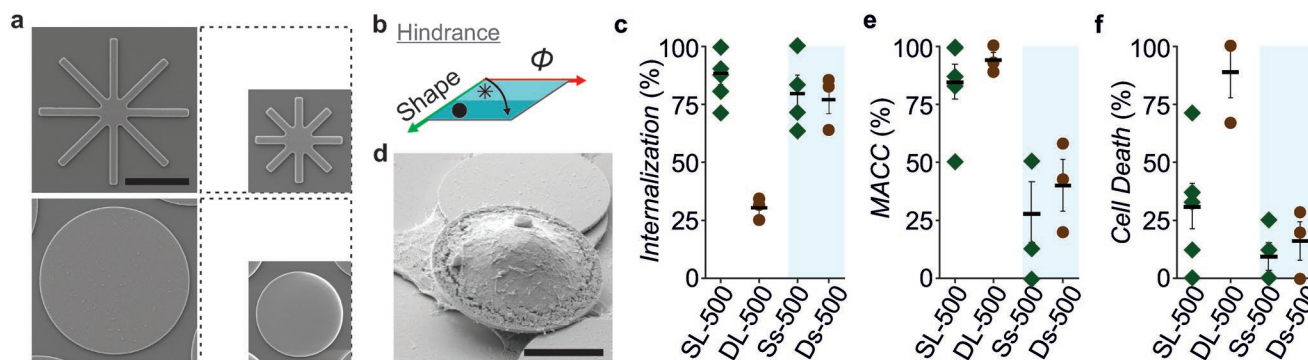


Figure 4. Hindrance effects in the cytoplasm. a) SEM images of fabricated SL, Ss, DL, and Ds devices. b) Expected hindrance effects on cells versus shape and Φ of the devices. c) Internalization rate for all the devices in HeLa cells. d) SEM image of a HeLa cell with an internalized DL-500. e,f) Percentages of MACC (e) and cell death (f) of HeLa cells with internalized devices. Each dot (c,e,f) represents an independent experiment where individual cells were followed for 24 h and the outcome plotted (Experimental Section, Supporting Information). The horizontal black lines represent the mean \pm s.e.m. Scale bars = 10 μm . Total number of analyzed cells, $n = 33\text{--}48$.

these smaller devices were located away from the center, they did not obstruct correct spindle positioning (Movie S6, Supporting Information). These results show that MACC and cell death due to hindrance effects are minimized if the devices are located away from the cell center.

However, intracellular hindrance is not only a function of device volume (Figure S3, Supporting Information). The volume of Ds-500 devices was $\approx 31\%$ greater than that of SL-500 even though SL-500 induced $\approx 94\%$ more cell death (Figure 4f). The disk-shaped devices show higher cell death rates even though they all have the same diameter, DL-500 induced $\approx 184\%$ more than SL-500 and Ds-500 $\approx 75\%$ more than star-shaped Ss-500. This suggests that device shape, rather than volume or diameter, is a major determinant of intracellular mechanical damage.

4.2. Intracellular Mechanical Device Stiffness as Dominant Factor to Alter Cell Cycle and Provoke Cell Death

We next tested the possibility that intracellular mechanical perturbation is also correlated with device stiffness, K . We predicted that if the device stiffnesses were sufficiently low, intracellular forces could bend the devices and place them to reduce

their mechanical impact on the cell, which is what had happened with relatively small star and disk devices. Experiments that study the elastic component of HeLa cells calculated an effective Young's modulus of ≈ 30 kPa,^[24] whereas polysilicon has a Young's modulus 10^6 times larger (≈ 169 GPa),^[25] which, in principle, suggests that the cells would experience great difficulty in bending internalized devices. However, high aspect ratio devices (Figure S3, Supporting Information) had reduced stiffness. For the same diameter, disk-shaped devices' stiffness was larger than that of star-shaped, and increased with thickness (Figure 5a). We fabricated devices with different thicknesses ($t = 487.0 \pm 1.2$, 241.6 ± 4.0 , 109.4 ± 2.0 , and 46.5 ± 0.4 nm), for which numerical simulations, by using finite element method (FEM), revealed a wide range of stiffness, from 19.4 ± 0.4 nN μm^{-1} for SL-050, to $(1.17 \pm 0.06) \times 10^6$ nN μm^{-1} for Ds-500 (Figure 5b and Figure S7 and the Experimental Section (Supporting Information)).

We evaluated mechanical perturbation induced by internalized large star-shaped (SL) devices of different thicknesses due to their reduced stiffness compared with the disk-shaped devices (Figure 5b). We found no significant differences among internalization rates at all thicknesses (Figure 5c). Most SL devices underwent perpendicular tip-first internalization and, in a minority of cases, planar cell surface internalization,

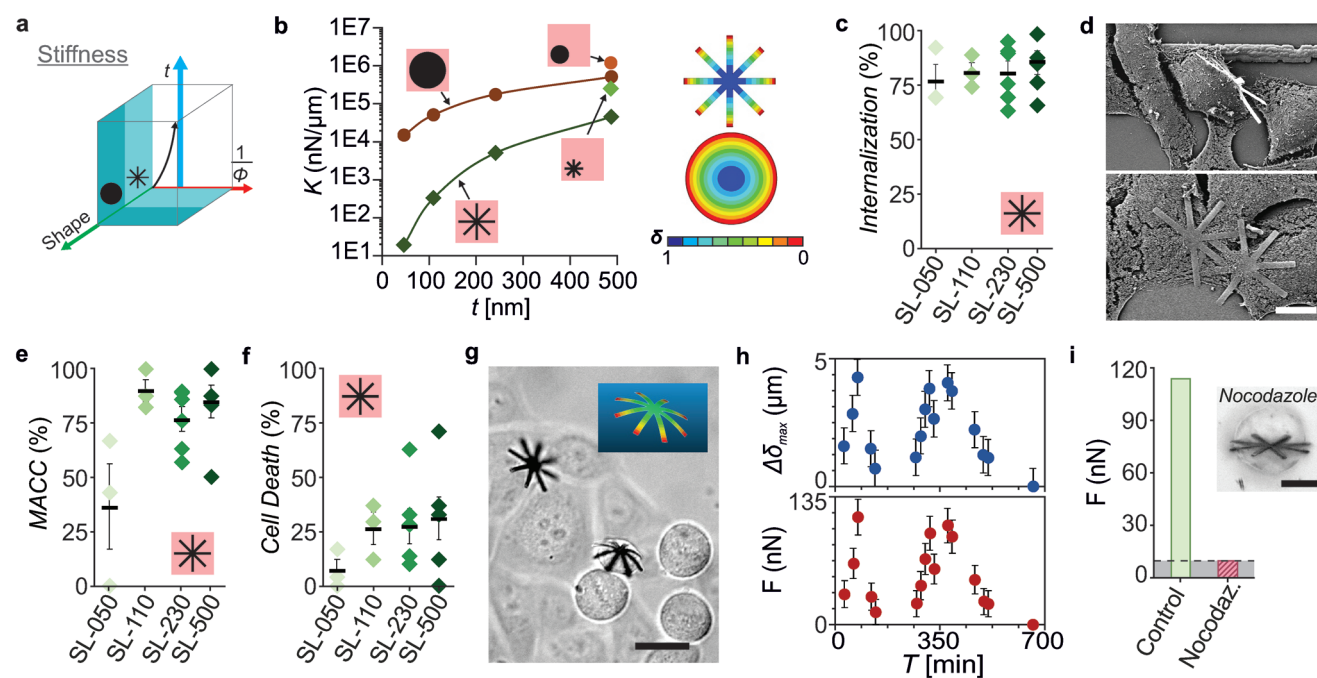


Figure 5. Stiffness effects in the cytoplasm (I). a) Schematic of stiffness effects on cells versus shape, t , and the $1/\Phi$ of the devices on cells. b) (Left) Finite element simulated stiffness of the devices versus thickness for the star- and disk-shaped devices (force load case). (Right) Normalized z-displacement of the structures. c) Internalization rate in HeLa cells for the SL devices with different thicknesses. Each dot represents an independent experiment where individual cells were followed for 24 h and the outcome plotted. d) HeLa cells internalizing SL-050 devices (top) by tip-first and (bottom) parallel showing multiple internalization points with the cell membrane. e) Percentages of MACC and f) cell death for the SL devices with different thicknesses. Each dot as in (c). g) Still optical image from a time lapse experiment showing a bended SL-050 device internalized inside a HeLa cell. (Inset) A normalized deformation of the device by FEM. h) (Top) Increment of device deformation, $\Delta\delta_{\text{max}}$, versus time, T , from (g) of a SL-050 device inside a HeLa cell and (bottom) the corresponding force to achieve $\Delta\delta_{\text{max}}$. i) Maximum intracellular force determined by SL-050 nanodevices for control and nocodazole-treated HeLa cells, and optical image of the minimum intensity projection of a SL-050 internalized in a HeLa cell treated with nocodazole. Each dot in (c,e,f) represents an independent experiment where individual cells were followed for 24 h and the outcome plotted (Experimental Section, Supporting Information). Horizontal black lines represent the mean \pm s.e.m. Scale bars = (d,i) $10 \mu\text{m}$ and (g) $20 \mu\text{m}$. Total number of analyzed cells, $n = 22\text{--}99$.

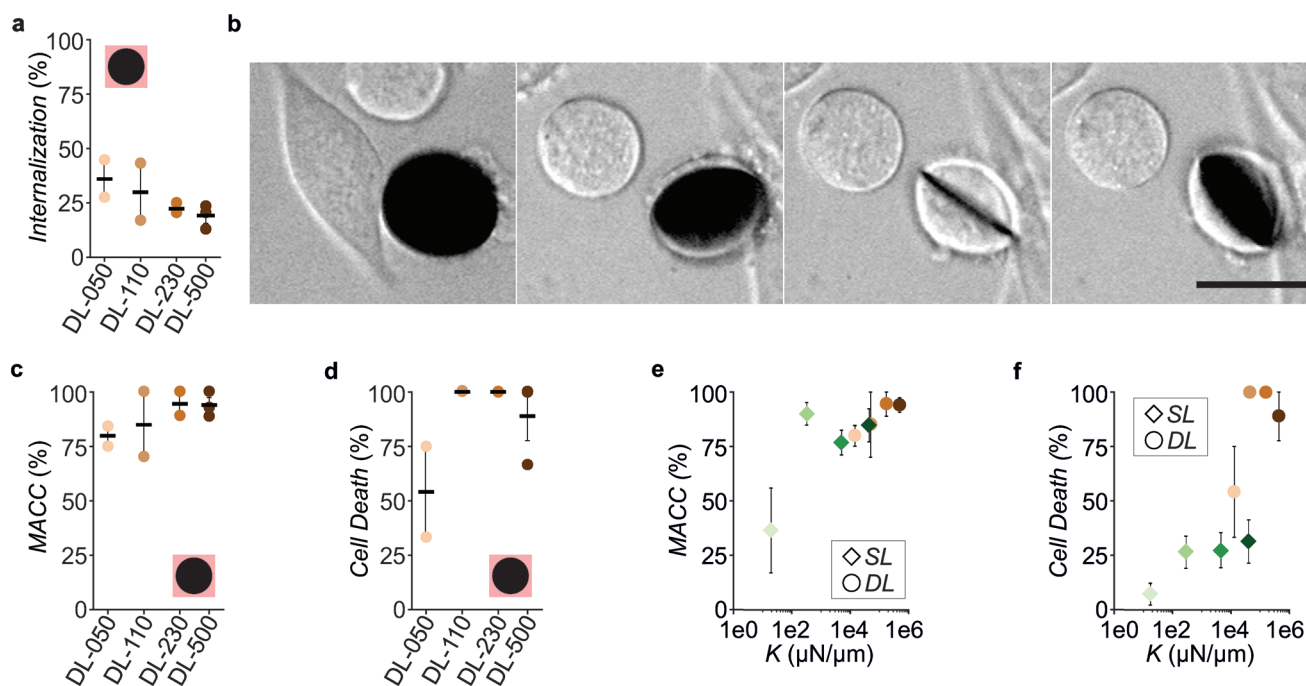


Figure 6. Stiffness effects in the cytoplasm (II). a) Internalization rate in HeLa cells for the DL devices with different thicknesses. b) Still optical images from a time lapse experiment of a HeLa cell with an internalized DL-500 device. Scale bar = 20 μm . c) Percentages of MACC and d) cell death for the DL devices with different thicknesses. e) MACC and f) cell death versus the device stiffness (force load model). Each dot in (a,c–f) represents an independent experiment where individual cells were followed for 24 h and the outcome plotted (Experimental Section, Supporting Information). The horizontal black lines represent the mean \pm s.e.m. Total number of analyzed cells, $n = 22\text{--}99$.

typically for SL-050 devices (Figure 5d) because their rigidity was small enough to allow bending at multiple points, and hence, more contacts or contacts with a bigger footprint. MACC and cell death (Figure 5e,f) were clearly smaller for SL-050 devices, which had the lowest stiffness (Figure 5b) and intracellular forces were sufficient to bend them during mitosis (Figure 5g and Movie S7 (Supporting Information)). On the contrary, MACC and cell death caused by thicker SL-110, SL-230, and SL-500 devices were similarly large (Figure 5e,f) and measurable device bending was not observed. This corroborates that cells cannot generate enough intracellular force to bend SL-110, SL-230, and SL-500 devices to relocate them in a less harmful position. The maximum intracellular mechanical load exerted by cells during mitosis, $F_{\text{mit,max}}$, is between 114 ± 19 and 160 ± 9 nN, which corresponds to the force to bend the SL-050 devices up to 4.3 ± 0.7 μm (Figure 5h) and the required force to bend the SL-110 device by ≥ 0.5 μm (minimum observable deflection, not detected for SL-110; Figure S7, Supporting Information), respectively.

Although comparison between studies are thwarted by technical differences, probe size, and hierarchical level, our intracellular force measurements were in agreement with extracellular confinement forces obtained by scanning force microscopy.^[26] Mitotic HeLa cells could withstand external confinement forces up to 100 nN before reaching heights that retard mitotic progression and forces over 150 nN blocked mitosis completely due to the mechanical perturbation of spindle geometry.^[26] Both values are in agreement with our intracellular measurements, indicating that the main force generator during large cell confinement is the spindle apparatus, as our intracellular

measurements are not affected neither by the intracellular hydrostatic pressure^[27] nor the reduced surface tension exerted by either the membrane and cortex.^[28]

To further demonstrate this reasoning, we performed a molecular perturbation experiment where we used 1×10^{-6} M nocodazole to destabilize microtubules and suppress their polymerization,^[29] preventing spindle formation but leading to cell rounding.^[30] Nocodazole was added after the SL-050 devices were internalized in HeLa cells and we observed that, in the absence of the spindle (Figure S8, Supporting Information), the nanodevices did not show an observable bending and hence a reduced intracellular force (Figure 5i), confirming that spindle and not the membrane–cortex system is the source of the intracellular forces that prevent confinement.

On the contrary, DL devices exhibited lower internalization rates for all thicknesses compared to star-shaped devices (Figure 6a), further suggesting that in the 50–500 nm range, shape, and not thickness, is the predominant factor for internalization. As with SL devices, DL devices typically occupied an equatorial position during cell division (Figure 6b), where the spindle would normally be; this is consistent with an average of $88.29 \pm 3.11\%$ of MACC produced by internalized disks of any thickness (Figure 6c). Cell death occurred in $96.30 \pm 3.70\%$ on average of cells containing DL devices ≥ 110 nm thick, and $54.17 \pm 20.83\%$ for DL-050 devices (Figure 6d). Therefore, only when the device stiffness was sufficiently low to permit device bending during division, MACC and cell death were diminished (Figure 6e,f). In addition, device shape is relevant to cell death, whose values were always larger for disks, and even in disks of reduced stiffness (DL-050) (Figure 6f).

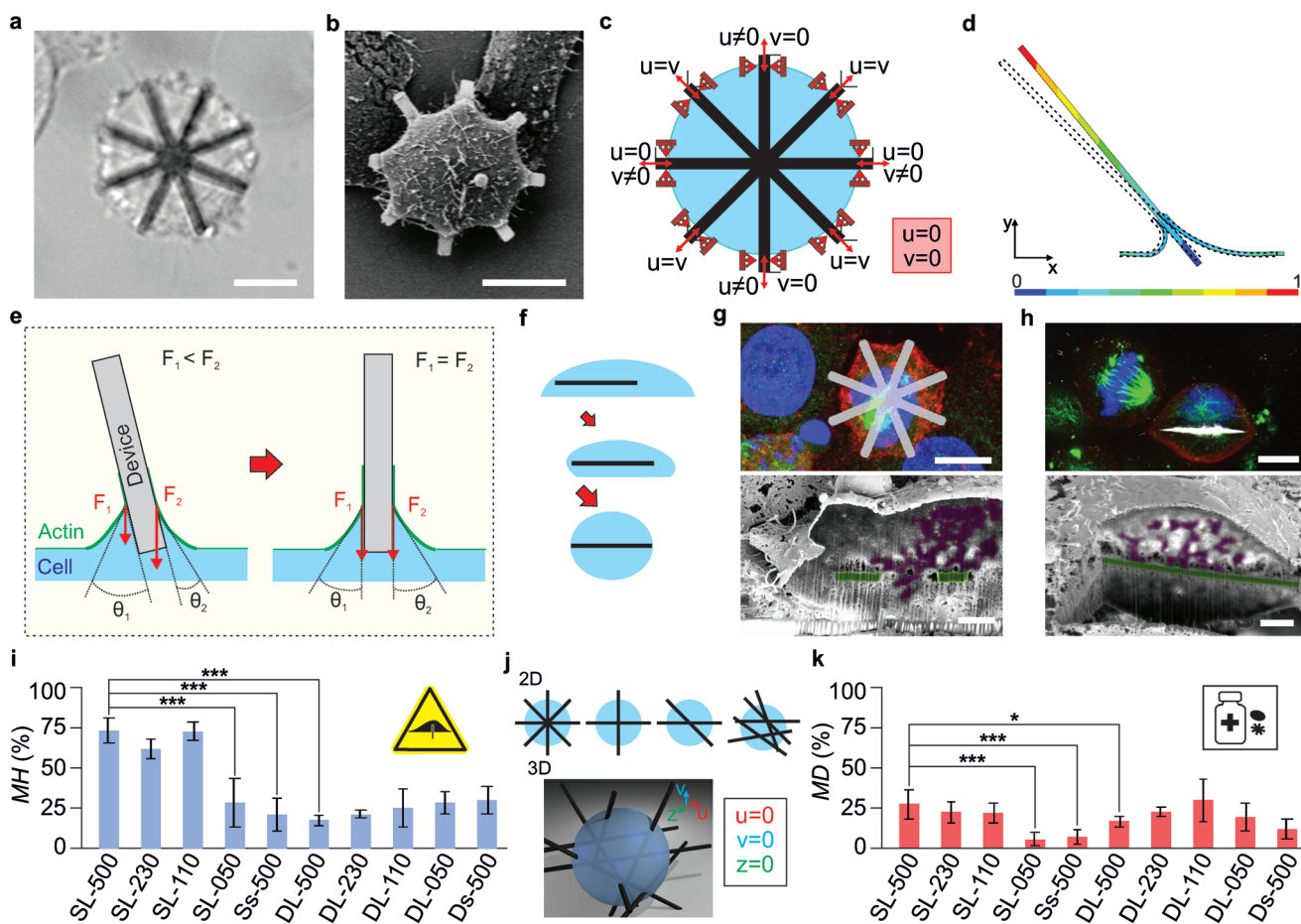


Figure 7. Maximization of the device mechanical disruption and their application to nanomedicine. a) Optical and b) SEM images of a HeLa cell during mitosis with an internalized and centered SL-500 and SL-050, respectively. c) Roller support constraints on the cell membrane for the star-shaped devices fixed the chips during mitosis. u and v represent local axis. d) A simulated and e) analytical force model based on the surface stress, γ , at the membrane–cortex system favoring perpendicular internalization of the chips. f) Gradient of effective stiffness (GES) model favoring cell centering. g,h) (Top) Confocal images of a cell stained with phalloidin for actin (red), tubulin for microtubules (green), and 4',6-diamidino-2-phenylindole (DAPI) for nuclei (blue); (bottom) SEM images of nanomachined cells with internalized SL-500 (g) and DL-500 (h) chips. i) Mechanical hazard (MH) index for all the devices. j) 2D and 3D combination of nonparallel 1D structures which overpass the cell diameter are fixed during mitosis. k) Mechanical death (MD) index for all the devices. Statistical comparisons between groups: $p < 0.05$, $** < 0.01$, and $*** < 0.0001$ (two-tailed Student's t -test). Scale bars = (a,b, top-g, top-h) 10 μm and (bottom-g, bottom-h) 1.5 μm .

4.3. Device Structural Support on Cell Membrane Causes Major Mitotic Perturbation

Although the volume of a HeLa cell is more than an order of magnitude smaller than the volume of a one-cell mouse embryo, we detected forces almost 10 times larger (114 vs 17.7 nN, respectively), and 1745 and 233 Pa when expressed in terms of pressure.^[15] This led us to consider the role played by structural support of the devices at the cell membrane, understood as the structural support of the cantilevers in the cortex that limits the device displacements.

Mechanical supports at the cell membrane fixed the position of internalized devices larger than the HeLa cell diameter, producing a robust mechanical perturbation during cell division. During mitotic rounding, the devices relocated (Figure 6b and Figure 7a,b). DL and SL devices were anchored by fixed supports to the cell membrane. Equivalent boundary condition is exhibited for the SL devices with cantilevers piercing the

membrane and taking off part of the cantilever, especially the thinnest ones (SL-050). Although individual cantilever supports could act as a roller, the nonparallel cantilever distribution also causes the global fixing of the devices (Figure 7c and Figure S9 (Supporting Information)). In agreement with this, cell expulsion of anchored intracellular devices was not observed in these cases. Thus, devices that exceed the cell diameter can become internalized and immobilized during mitosis. Cell responses to these configurations mimic those induced by cell-internalized meshes of 1D and 2D materials.^[9]

We also asked why DL and SL devices tend to position close to the cell equator during division, a positioning that clearly becomes a critical mechanical obstacle for productive mitotic spindle positioning. We propose that centering is a response to multiple phenomena. Actin-mediated internalization would favor internalization perpendicularly to the membrane.^[13] Indeed, we observed cortical actin accumulation during internalization in contact with the chips (Figure 2b). Moreover, the

generation of protrusive forces due to surface tension of the membrane–cortex system^[19] would also facilitate perpendicular internalization.^[13] A simple qualitative Newton formulation, corroborated by FEM, further suggested that if a device is internalized obliquely with respect to the tensioned membrane–cortex system, with different contact angles θ_1 and θ_2 , unbalanced forces will be induced that favor perpendicular internalization (Figure 7d,e and Figure S9 and the Experimental Section (Supporting Information)). Once internalized, a gradient of effective stiffness (GES) contributes to device centering, further inducing device convergence toward the center, where the cytoplasmic effective stiffness is lower^[15] (Figure 7f and Figure S9 (Supporting Information)).

Overall, the tendency of the devices to be located at the cell equator during cell rounding is predicted to hinder spindle centering and chromosome alignment, both of which are essential for normative cytokinesis.^[31] We accordingly observed spindles and the chromosomes intertwined with the arms of SL designs (Figure 7g). DL devices apparently excluded the spindle and chromosomes to one of the cell hemispheres (Figure 7h and Figure S10 and Movie S8 (Supporting Information)). Even if the spindle can be mounted in one hemisphere (Figure 7h, top and Figure S10 (Supporting Information)), the cell division would be compromised as it is taking place in a confined space.^[26,31–33]

5. Intracellular Mechanical Drugs toward Nanomedicine

Internalization rates, MACC, and cell death are parameters that should be considered together when evaluating the toxicity of physical objects or their future use as physical drugs. When cells are exposed to mechanical objects, the damage they undergo reflects both their capacity to internalize them and their intracellular consequences. To assess this, we defined a “mechanical hazard (MH)” index by multiplying the internalization rate for each device and its associated MACC. This suggests that large, stiff, star-shaped devices have the largest MH indices (Figure 7i), due to relatively large internalization rates (Figures 4c, 5c, and 6a). This could be extended to demonstrate the potential mechanical toxicity of materials composed of meshes of 1D structures, such as nanofibers (i.e., asbestos), nanowires, or 2D and 3D materials with parts of their geometry that mimic 1D structures (Figure 7j) and may facilitate internalization, while meshes increase the stiffness and anchor the structure to the cortex. In spite of the strong MACC effects of large disk devices, because their internalization rate is low, their MH indices are low and comparable to those of disks and stars with smaller diameter. Barriers to internalizing larger structures are presumably a constitutive mechanism to avoid a large intracellular mechanical toxicity. However, large 2D structures with parts that resemble 1D structures are clearly able to circumvent this barrier and elicit increased mechanical toxicity.

Notwithstanding considerable research effort, there remains a lack of cell mechanics applications to biomedicine in a manner that is analogous to chemical drugs. Mechanical devices acting as physically rather than chemically based drugs could meet criteria required of functional biomaterials designed to steer cell fate and function in prescribed directions.^[34] With this in mind,

it may be possible to evaluate devices as mechanical agents that kill cells. To achieve this, we propose a mechanical death index, MD = internalization rate \times cell death rate. Outstandingly, MD is similar for SL-500 and DL-500 devices (Figure 7k), yet with higher cell death rates for the latter (Figures 4f, 5f, and 6d). Anyway, devices have to be stiff enough to increase their cell-killing capability by interfering in the spindle localization and mounting (Figure 7k). Remarkably, it has to be considered that most surviving cells with blocked mitosis or failed cytokinesis could die after the last observational time point (Movie S9 (Supporting Information)). Thus, these results suggest a potential application of the mechanical drugs to kill cells, which will require studies covering longer times to evaluate the fitness of daughter cells.

6. Discussion

Current advances in materials science have demonstrated that extracellular mechanical cues can define cell function and cell fate; here, we determined how intracellular mechanical cues produce similar effects. We have shown that the use of highly reproducible intracellular nanomechanical drugs, that can be precisely tuned in shape, dimensions, and stiffness, allows the study of how intracellular physical structures interfere mechanically with cell function, contributing to better understanding cell physiology and disease.

In this context, our results show that nonphagocytic HeLa cells can internalize nanostructures with diameters that exceed their mitotic diameter and those with parts akin to 1D structures are more easily internalized. In the case of phagocytic cells, there is controversy about their capacity to sense size, shape, and rigidity of the engulfed target.^[22] For HeLa cells, the predominant parameters guiding internalization are shape and diameter, with almost no effect of thickness in the range 50–500 nm. This agrees with previous studies on HeLa cells using smaller particles, of $\approx 5 \mu\text{m}$ diameter.^[35] On the contrary, no significant dependence for uptake efficiency on target rigidity is observed (Figure 5b,c and Figure S7 (Supporting Information)). It is important to distinguish between global device rigidity, which can be low, and their local rigidity due to the high Young's modulus of polysilicon ($Y_{\text{polysilicon}} = 169 \text{ GPa}$), which is too high for molecular forces to locally deform polysilicon and hence beyond the mechanosensitive range of the cell.^[22]

Our results also show that intracellular structures exceeding the HeLa cell diameter were fixed at the cell membrane–cortex system during mitosis and physically tend to occupy the equator during spindle formation and chromosome alignment. These results could be extrapolated to any combination of non-parallel internalized 1D nanostructures that are able to form a 2D or 3D mesh exceeding the mitotic diameter, in which the overall mechanical boundary conditions can be reduced to zero displacements (Figure 7c,j). In these cases, nanomeshes formed by 1D nanomaterials (i.e., bundles of fibers), would exhibit increased nanotoxicity, as the internalization is favored by the individual long nanostructures, but rigidity once inside cells is increased by the entanglement of individual 1D structures and by the boundary conditions at the cell membrane–cortex system.

Structures smaller than the cell diameter or with a stiffness below a certain magnitude can be displaced or deformed inside the cell to positions far from the spindle mounting and chromosome alignment, and consequently reduce the MACC and the cell death. Conversely, control and nocodazole-treated HeLa cells with nanodevices report that spindle formation is able to generate limited forces, up to 114 nN, to reduce intracellular mechanical confinement. This value is similar to the reported extracellular force of 150 nN to block mitosis due to the mechanical perturbation of spindle geometry on HeLa cells.^[26] This agreement indicates that the main force generator during extracellular cell confinement is the spindle apparatus and demonstrates that intracellular chips complement extracellular techniques in order to study the hierarchy of forces in cell mechanics.

The results can go beyond HeLa cell line, as additional cell types exhibited device internalization and affectation (Figure S11, Supporting Information). The fabrication technology offers the possibility to fabricate devices with different shapes and dimensions in order to better understand universal cell internalization, mechanical affectation on cell cycle and cell death and to avoid or promote devices as drug delivery carriers.^[23,36]

The results presented here also provide new insights into future mechanical therapeutics. By the design and reproducible manufacture of precision devices, we may be able to perform prescribed intracellular functions, including the induction of cell death or differentiation. Although, the cell-specific delivery may be a challenge, the mass production of mechanical drugs could be used to kill cancer cells, being their topical use an initial opportunity to explore. While cytokinetic failure can also promote tumorigenesis, the relative chromosomal instability and more rapid division of cancer cells may amplify the effect of mechanical drugs upon them.

To conclude, in contrast to extracellular mechanical tools, internalized mechanical drugs induce an alteration of intracellular boundary conditions, which redistributes the internal cell force balance and induces a rearrangement of the cell mechanical elements. Such intracellular mechanical drugs promise a wide range of possible developments to open new avenues of fundamental study, for instance, by mechanically controlling gene regulation or cell differentiation,^[37] but also, understanding how intracellular chips affect the cells will pave the way to new therapeutic options. The results show that intracellular chips are an innovative contribution to the semiconductor field as intracellular mechanical sensors, but also as intracellular actuators.

Supporting Information

Supporting Information is available from the Wiley Online Library or from the author.

Acknowledgements

M.I.A., M.D., A.H.-P., and P.V. contributed equally to this work. The authors are grateful to A. C. F. Perry for his constructive comments during manuscript preparation. This work was supported with funds from the Spanish Government Grant PID2020-115663GB-C3 funded by

MCIN/AEI/10.13039/501100011033/ and TEC2017-85059-C3 funded by MCIN/AEI/10.13039/501100011033/ and by FEDER “EU ERDF, a way of making Europe”. The authors thank the clean-room staff of IMB-CNM for fabrication of the microparticles and A. Sánchez for the nanomachining of the cells. The authors at CIB Margarita Salas are deeply indebted with the “Confocal Laser and Multidimensional Microscopy” in vivo in-house facility for their excellent work and professional collaboration.

Note: The email address for Teresa Suárez was corrected on April 27, 2022, after initial publication online.

Conflict of Interest

The authors declare no conflict of interest.

Data Availability Statement

The data that support the findings of this study are available from the corresponding author upon reasonable request.

Keywords

biomaterials, cell cycle, mechanobiology, nanomaterials, nanomedicine, silicon chips

Received: November 24, 2021

Revised: February 1, 2022

Published online: March 21, 2022

- [1] D. E. Ingber, N. Wang, D. Stamenović, *Rep. Prog. Phys.* **2014**, *77*, 046603.
- [2] D. A. Fletcher, R. D. Mullins, *Nature* **2010**, *463*, 485.
- [3] Z. Meng, T. Moroishi, K. L. Guan, *Genes Dev.* **2016**, *30*, 1.
- [4] M. A. Jordan, L. Wilson, *Nat. Rev. Cancer* **2004**, *4*, 253.
- [5] D. Zhou, K. Zhao, W. Ping, J. Ge, X. Ma, L. Jun, *J. Am. Sci.* **2005**, *1*, 55.
- [6] M. Trendowski, *Biochim. Biophys. Acta, Rev. Cancer* **2014**, *1846*, 599.
- [7] A. Janssen, R. H. Medema, *Nat. Cell Biol.* **2011**, *13*, 199.
- [8] M. Krajcovic, N. B. Johnson, Q. Sun, G. Normand, N. Hoover, E. Yao, A. L. Richardson, R. W. King, E. S. Cibas, S. J. Schnitt, J. S. Brugge, M. Overholtzer, *Nat. Cell Biol.* **2011**, *13*, 324.
- [9] C. G. Jensen, L. C. W. Jensen, C. L. Rieder, R. W. Cole, J. G. Ault, *Carcinogenesis* **1996**, *17*, 2013.
- [10] E. Fernandez-Rosas, R. Gómez, E. Ibañez, L. Barrios, M. Duch, J. Esteve, C. Nogués, J. A. Plaza, *Small* **2009**, *5*, 2433.
- [11] R. Gómez-Martínez, P. Vázquez, M. Duch, A. Muriano, D. Pinacho, N. Sanvicens, F. Sánchez-Baeza, P. Boya, E. J. de la Rosa, J. Esteve, T. Suárez, J. A. Plaza, *Small* **2010**, *6*, 499.
- [12] R. Gómez-Martínez, A. M. Hernández-Pinto, M. Duch, P. Vázquez, K. Zinoviev, E. J. de la Rosa, J. Esteve, T. Suárez, J. A. Plaza, *Nat. Nanotechnol.* **2013**, *8*, 517.
- [13] X. Shi, A. von dem Bussche, R. H. Hurt, A. B. Kane, H. Gao, *Nat. Nanotechnol.* **2011**, *6*, 714.
- [14] Y. Shao, J. Fu, *Adv. Mater.* **2014**, *26*, 1494.
- [15] M. Duch, N. Torras, M. Asami, T. Suzuki, M. I. Arjona, R. Gómez-Martínez, M. D. VerMilyea, R. Castilla, J. A. Plaza, A. C. F. Perry, *Nat. Mater.* **2020**, *19*, 1114.
- [16] J. Fan, P. K. Chu, *Small* **2010**, *6*, 2080.
- [17] N. Torras, J. P. Aguiló, P. Vázquez, M. Duch, A. M. Hernández-Pinto, J. Samitier, E. J. de la Rosa, J. Esteve, T. Suárez, L. Pérez-García, J. A. Plaza, *Adv. Mater.* **2016**, *28*, 1449.
- [18] J. R. Masters, *Nat. Rev. Cancer* **2002**, *2*, 315.

- [19] V. Jaumouillé, C. M. Waterman, *Front. Immunol.* **2020**, *11*, <https://doi.org/10.3389/fimmu.2020.01097>.
- [20] J. C. Seeberg, M. Loibl, F. Moser, M. Schwegler, M. Büttner-Herold, C. Daniel, F. B. Engel, A. Hartmann, U. Schlötzer-Schrehardt, M. Goppelt-Strube, V. Schellerer, E. Naschberger, I. Ganzleben, L. Heinzerling, R. Fietkau, L. V. Distel, *Sci. Rep.* **2019**, *9*, 11875.
- [21] M. X. Yang, X. Hu, D. Akin, A. Poon, H.-S. P. Wong, *Sci. Rep.* **2021**, *11*, 5967.
- [22] D. Vorselen, Y. Wang, M. M. de Jesus, P. K. Shah, M. J. Footer, M. Huse, W. Cai, J. A. Theriot, *Nat. Commun.* **2020**, *11*, 20.
- [23] J. A. Champion, S. Mitragotri, *Proc. Natl. Acad. Sci. USA* **2006**, *103*, 4930.
- [24] S. Loporatti, D. Vergara, A. Zacheo, V. Vergaro, G. Maruccio, R. Cingolani, R. Rinaldi, *Nanotechnology* **2009**, *20*, 055103.
- [25] W. N. Sharpe, B. Yuan, R. Vaidyanathan, R. L. Edwards, in *Proc. IEEE Tenth Annual Int. Workshop on Micro Electro Mechanical Systems. An Investigation of Micro Structures, Sensors, Actuators, Machines and Robots*, IEEE, Piscataway, NJ, USA **1997**, pp. 424–429.
- [26] C. J. Cattin, M. Düggelin, D. Martinez-Martin, C. Gerber, D. J. Müller, M. P. Stewart, *Proc. Natl. Acad. Sci. USA* **2015**, *112*, 11258.
- [27] M. P. Stewart, J. Helenius, Y. Toyoda, S. P. Ramanathan, D. J. Muller, A. A. Hyman, *Nature* **2011**, *469*, 226.
- [28] P. Chugh, A. G. Clark, M. B. Smith, D. A. D. Cassani, K. Dierkes, A. Ragab, P. P. Roux, G. Charras, G. Salbreux, E. K. Paluch, *Nat. Cell Biol.* **2017**, *19*, 689.
- [29] J. Lu, *Am. J. Life Sci.* **2018**, *6*, 7.
- [30] R. J. Vasquez, B. Howell, A. M. C. Yvon, P. Wadsworth, L. Cassimeris, *Mol. Biol. Cell* **1997**, *8*, 973.
- [31] C. Cadart, E. Zlotek-Zlotkiewicz, M. Le Berre, M. Piel, H. K. Matthews, *Dev. Cell* **2014**, *29*, 159.
- [32] O. M. Lancaster, M. Le Berre, A. Dimitracopoulos, D. Bonazzi, E. Zlotek-Zlotkiewicz, R. Picone, T. Duke, M. Piel, B. Baum, *Dev. Cell* **2013**, *25*, 270.
- [33] H. T. K. Tse, W. M. C. Weaver, D. Di Carlo, *PLoS ONE* **2012**, *7*, e38986.
- [34] M. Darnell, D. J. Mooney, *Nat. Mater.* **2017**, *16*, 1178.
- [35] S. E. A. Gratton, P. A. Ropp, P. D. Pohlhaus, J. C. Luft, V. J. Madden, M. E. Napier, J. M. DeSimone, *Proc. Natl. Acad. Sci. USA* **2008**, *105*, 11613.
- [36] M. P. Stewart, A. Sharei, X. Ding, G. Sahay, R. Langer, K. F. Jensen, *Nature* **2016**, *538*, 183.
- [37] T. Panciera, A. Citron, D. Di Biagio, G. Battilana, A. Gandin, S. Giullitti, M. Forcato, S. Bicciato, V. Panzetta, S. Fusco, L. Azzolin, A. Totaro, A. P. Dei Tos, M. Fassan, V. Vindigni, F. Bassetto, A. Rosato, G. Brusatin, M. Cordenonsi, S. Piccolo, *Nat. Mater.* **2020**, *19*, 797.